*Journal of The Electrochemical Society*, **164** (14) A3785-A3792 (2017)
0013-4651/2017/164(14)/A3785/8/$37.00 © The Electrochemical Society


# EQCM and RDE/RRDE Study of Soluble Iron Phthalocyanine Bifunctional Catalyst for the Lithium-Oxygen Battery

**W. R. Torres, F. Davia, M. del Pozo, A. Y. Tesio, and E. J. Calvo**[z]

*INQUIMAE-CONICET-Facultad de Ciencias Exactas y Naturales, Universidad de Buenos Aires, Ciudad Universitaria, Buenos Aires 1428, Argentina*

Soluble iron phtalocyanine (FePc) has been studied as a bifunctional catalyst for the oxygen reduction reaction (ORR) and oxygen evolution (OER) in lithium air cathodes by means of electrogravimetry with shear wave dissipation, cyclic voltammetry (CV) and rotating ring disk electrode (RRDE). The oxygen reduction reaction (ORR) has been studied on Au in oxygen saturated TBA-$PF_6$ in DMSO and LiTFSI-DMSO electrolyte for increasing concentration of Fe-phtalocyanine as redox mediator for the two-electron ORR at 2.2 V and the oxidation of the surface $Li_2O_2$ product below 3.6 V vs. $Li/Li^+$ where the solvent is stable. The soluble FePc catalyst promotes the ORR solution phase mechanism.


Manuscript submitted September 18, 2017; revised manuscript received November 25, 2017. Published December 13, 2017.

There is a great attention on the lithium-oxygen battery at least theoretically as a high energy density option for electric vehicle applications with long driving range. Several solid catalysts have failed to avoid the lithium-oxygen battery cathode capacity fading over continuous cycling. Soluble redox couples have been proposed to circumvent this problem. Zecevic et al. filed a patent on the use of soluble redox oxygen evolving catalysts.[1] Among the soluble redox shuttles that have been reported are tetrathiafulvalene (TTF/TTF$^+$),[2–4] ethylviologen,[5–7] tri-iodide ($I_3^-/I_2$)[8] and tris(2,4,6-trichlorophenyl) methyl (TTM),[9] quinones,[10] etc. A dual catalyst combining ethyl viologen and LiI has been recently discussed.[11]

The group of professor Goodenough has reported that soluble iron phthalocyanine (FePc) in DMSO and polyether solvents may act as a soluble bifunctional catalyst both for the oxygen reduction as well as for the oxidation of lithium peroxide at low overpotential.[12] The molecule exhibits two redox couples Fe(III)/Fe(II) and Fe(II)/Fe(I) that are able to catalyze the reduction of oxygen and the chemical oxidation of lithium peroxide by electrochemically produced Fe(III)Pc at relatively low overpotential. In the soluble mediator strategy the redox potential of the soluble mediator should be slightly higher than the equilibrium potential of the $O_2/Li_2O_2$ reaction, i.e. >2.96 V. The oxidized form of the redox catalyst should be capable of efficiently decomposing $Li_2O_2$ and the reduced form should be oxidized at the electrode surface uncovered by the non-conducting lithium peroxide. Another requirement for the soluble redox mediator is that it must not react with electrolyte/solvent or the Li metal anode.

More recently the group of professor Abraham introduced a solid phase FePc prepared by pyrolysis of iron(II) phtalocyanine embedded in high surface area carbon and demonstrated catalysis of ORR and OER in $Li^+$ containing non-aqueous electrolytes.[4]

There is ample literature on the FePc as electrocatalyst for the 4-electron ORR in aqueous solutions in connection with the fuel cell technology. FePc has been discovered to catalyze the ORR by Jahnke and Schonborn in the 60's.[13] Savy reported the highest activity for oxygen reduction for FePc in aqueous solutions ;[14,15] subsequently van Veen and Visser[16] confirmed that FePc dispersed on high-area carbons was active for the $O_2$ reduction both in alkaline and acid aqueous solutions. Beck suggested that the first step in the electrocatalysis was the formation of FePc-$O_2$ adduct with partial metal to $O_2$ charge transfer.[17] Later quantum mechanical calculations predicted that the Fe(III)-$O_2$ would have an optimum electronic configuration for the subsequent activation and reduction of $O_2$.[18] The oxygen bonding would involve the charge transfer from the electron-rich Fe(II) center to the oxygen $\pi^*$ orbital. A mechanistic study of $O_2$ reduction to water by soluble sulfonated FePc (FeTSPc) adsorbed on graphite electrodes was published by Zagal et al. in 1980.[19] The main feature of this mechanism is the role of Fe(III)/Fe(II) redox couple, with ORR taking place at the Fe(II) reduced FeTSPc. More recently, Tanaka et al.[20] reported Mössbauer and infrared spectroscopic and electrochemical studies of two μ-oxo iron phtalocyanine derivatives and FePc dispersed on carbon supports with redox processes which have been ascribed to the redox couples Fe(III) TsPc(−2) /Fe(II)TsPc(−2) and Fe(II)TsPc(−2)/Fe(I) TsPc(−2) in good agreement with redox potentials reported by Zecevic[21] and Zagal.[19] While all these data for the ORR have been obtained in aqueous electrolyte, for the Li-$O_2$ battery cathode the reaction takes place at less positive potentials in aprotic solvents in the vicinity of the Fe(II)/Fe(I) redox potential.

In the present communication we report new experimental results of EQCM electrogravimetry[22] and RRDE detection of soluble superoxide[23] on Au in LiTFSI-DMSO electrolyte and compare with the same reaction in the absence of lithium ions in the electrolyte. Furthermore, we discuss the possible mechanism of soluble FePc bifunctional catalyst in lithium-oxygen battery cathodes.

## Experimental

***Chemicals.***—Anhydrous dimethyl sulfoxide (DMSO), ≥99.9%, lithium bis(trifluro-methane) sulfonimide (LiTFSI) battery grade, ≥99.99% were obtained from SIGMA-ALDRICH and stored in the argon-filled MBRAUN glove box with the oxygen content ≤ 0.1 ppm and water content below 1.5 ppm. DMSO was dried for several days over molecular sieves, 3 Å (SIGMA-ALDRICH). All solutions were prepared inside the glove box and the water content was measured using the Karl Fisher 831 KF Coulometer (Metrohm) with typically 30 ppm of water at the beginning of the experiment. Long term experiments were avoided since after few hours of experimentation even with precautions the lithium salt in DMSO absorbs water from the ambient. Therefore freshly prepared solutions and short exposure to dry air were preferred.

***Eqcm cell.***—The electrochemical cell was built all in Teflon and the 10 MHz quartz crystal (Intl. Crystal Manufacturer, Oklahoma) were coated with 0.2 $cm^2$ gold disks (with 200 nm Au on titanium adhesion layer), placed at the bottom and filled with the electrolyte. DuPont Kalrez perfluoro elastomeric AS568 o-rings were used in DMSO solutions.

***EQCM measurements.***—Crystal admittance spectra in the vicinity of the fundamental resonant frequency, $f_o$, were acquired using a Hewlett Packard HP E5100A network analyzer connected to the quartz crystal in the Teflon electrochemical cell through 50 Ω coaxial matched cables (HP10502A) via a HP 41900A π- Network test fixture with rigid brass connectors to the crystal. The HP E5100A network analyzer was interfaced to a computer via Agilent 82357B USB/GPIB interface and the electrochemical cell was controlled with a grounded working electrode by means of an operational amplifier potentiostat/galvanostat with special software developed in the laboratory using Labview 10.0 (National). The working electrode was

[z]E-mail: calvo@qi.fcen.uba.ar

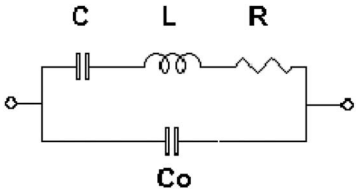


**Scheme 1.** Buterworth-Van Dyke (BVD) electrical equivalent circuit for quartz crystal.

isolated by means of a series 4.7 nF capacitor, the electrochemical current was measured at the auxiliary electrode and both current and potential signals were acquired by 2 Agilent 34410 61/2 digit multimeters by USB interfaces. The network analyzer was calibrated prior to each measurement by 3-term calibration: open, close and 50 Ω. The acoustic admittance spectra of the Au covered quartz crystal were recorded at 1.5 s intervals simultaneously to current and potential signals for the oxygen reduction reaction (ORR).

The electrical complex admittance of the Buterworth van Dyke (BVD) equivalent electrical circuit of Scheme 1 is:

$$Y(\omega) = G(\omega) + jB(\omega) \quad [1]$$

where the real part G(ω) is the conductance and the imaginary part B(ω) the susceptance of the quartz crystal admittance is given in terms of the BVD elements:

$$G = \frac{R}{R^2 + \left(\omega L - \frac{1}{\omega C}\right)^2} \quad and \quad B = \omega C_o - \frac{\left(\omega L - \frac{1}{\omega C}\right)}{R^2 + \left(\omega L - \frac{1}{\omega C}\right)^2} \quad [2]$$

with $j = \sqrt{-1}$ and $\omega_o = 2\pi f_o$ defines the series resonant frequency of the quartz crystal with a maximum conductance $G(\omega_o)_{max} = 1/R$ at the resonant frequency. (see data in Supporting Information).

The resistance, R, represents all the energy losses of the shear wave penetrating the liquid and surface film or surface particle asperities as well as losses in the o-ring support. Typical values of $R_q = 40$ Ω (including O-ring and crystal fitting), Lq = 8.5 mH, Cq = 30 fF, and $C_0 = 5$ pF for 10 MHz crystals in air with ωL (total) ~535,000 Ω were obtained and experimentally verified.

For low crystal load by the surface deposit ($Z_L << Z_Q$) a lumped element circuit can be approximated and the shift in the quartz impedance due to the ORR products deposit can be written:

$$\Delta Z = \Delta R + j\Delta(\omega L) \quad [3]$$

where ΔR and Δ(ωL) are the real and imaginary parts of the impedance shift with respect to the initial quartz crystal condition before the beginning of the ORR process.

For acoustically thin deposits, the Saurbrey equation relates the resonant frequency shift with the areal mass of deposit:[24]

$$\Delta f = -\frac{\left(2f_0^2\right)}{\sqrt{\left(\rho_Q \mu_Q\right)}} \cdot \frac{\Delta m}{A} \quad [4]$$

Δf is the measured frequency shift, Δm the mass loading, A the piezoelectrically active area, the quartz density ($\rho_Q = 2.648$ g.cm$^{-3}$) and the shear modulus of AT-cut quartz ($\mu_Q = 2.947 \times 10^{11}$ dyn cm$^{-2}$). The sensitivity factor increases at high resonant frequency of the resonator which corresponds to a thinner quartz crystal; for example a 10 MHz AT-cut quartz crystal 0.017 cm thick has a nominal sensitivity of 0.226 Hz cm$^2$ .ng$^{-1}$.

For acoustically thin films (ΔR→0), the equivalent of Eq. 4 is:

$$\Delta(\omega L) = \Delta X_L = -\frac{\pi Z_Q \Delta f}{f_o} = \frac{2\pi Z_Q \Delta m}{\sqrt{\left(\rho_Q \mu_Q\right)} A} = 4.6x10^{-8}\frac{\Delta m}{A} \quad [5]$$

with the conversion factor $4.6 \times 10^{-8}$ g.cm$^{-2}$.Ω$^{-1}$ calibrated by electrodeposition of copper on Au and the deposited mass calculated from the number of moles deposited with the Faraday law of electrolysis and the molar mass.

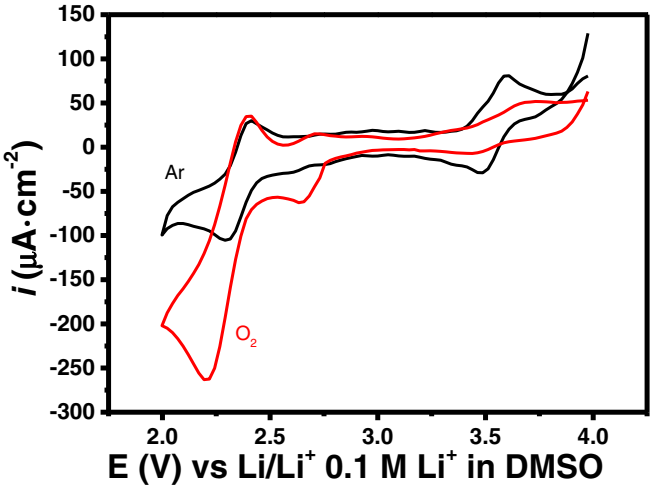


**Figure 1.** Cyclic scan voltammetry of 2 mM FePc in 0.1M TBA-$PF_6$ in DMSO in Ar-saturated (black) and $O_2$ saturated solution (red) at a 0.2 cm$^2$ Au disk electrode at v = 20 mV.s$^{-1}$.

***RRDE measurements.***—A rotating Au-ring Au-disk electrode (RRDE) embedded in Araldite (Ciba-Geigy) epoxy resin cylindrical body was employed with the following geometry: $r_1 = 0.25$ cm, $r_2 = 0.26$ cm , $r_3 = 0.30$ cm and a collection efficiency $N_0 = 0.28$. The geometrical area of the disk electrode was in all cases 0.196 cm$^2$. Soluble superoxide was detected at the ring electrode by convective-diffusion oxidation current at $E_R = 3.0$ V vs Li/Li$^+$ in DMSO.

A non-aqueous reference electrode made with a Pt wire coated with equimolar $LiMn_2O_4$/ $Li_2Mn_2O_4$ (3.25 V vs. Li/Li$^+$) in the same electrolyte and potentials herein are referred to the Li/Li$^+$ scale electrode in 0.1 M $LiPF_6$ in DMSO. It should be noted that the Li/Li$^+$ electrode potential is very solvent dependent,[25,26] i.e., Ag/Ag$^+$ vs. Li/Li$^+$ (0.1 M $LiPF_6$) varies from 3.23 V in acetonitrile to 3.70 V in DMSO. A 1 cm$^2$ platinum gauze (Johnson Matthey) was employed as counter electrode.

## Results and Discussion

In oxygen free solutions, two redox processes of soluble FePc on Au in DMSO containing 0.1M TBA-$PF_6$ are observed in Figure 1: (i) at 3.53 V, and (ii) at 2.35 V respectively. These have been described in the literature:[27] peak I corresponds to the reversible FePc(III)/FePc(II) system, peak II to FePc(II)/FePc(I) and the reduction of the axial ligand, for FePc(I)/FePc(I)(−3), is observed below 1.90 V (not shown) as reported by Lever and Wilshire for FePc in DMSO solutions containing LiCl.[27] Ercolani and co-workers studied the interaction of (phthalocyaninato) iron(II) with $O_2$ and reported the synthesis and characterization of two different crystalline forms of a (μ-oxo)bis-(phthalocyaninato) iron (III),FePc-O-FePc.[28] Tanaka has shown that these two μ-oxo FePc dispersed on carbon underwent the two redox processes Fe(III)/Fe(II) and Fe(II)/Fe(I) in an aqueous environment.[20]

The axial ligand in FePc plays a key role in particular with non-aqueous solvents with strong donor properties such as DMSO, pyridine, etc. which act as axial ligands and modulate the redox potentials.[29]

If the DMSO-TBA solution is saturated in $O_2$, a cathodic peak coincident with the second redox couple due to Fe(II)/Fe(I) with a small pre-peak is observed. The axial DMSO bound to the $d_z^2$ iron orbital can be replaced by oxygen if the resulting adduct Fe-$O_2^-$ is negatively charged and displaces the DMSO axial ligand. Figure 1 shows a similar ORR pattern as described by Sun et al.[12]

Rotating disk electrode studies (see supporting information) have shown convective-diffusion waves for both $Fe^{III}/Fe^{II}$ and $Fe^{II}/Fe^{I}$ redox couples, and the analysis of the limiting currents with the Levich equation for n = 1, $\nu_{DMSO} = 0.0019$ cm$^2$s$^{-1}$ $C_{PcFe} = 2 \times 10^{-6}$ mol.cm$^{-3}$

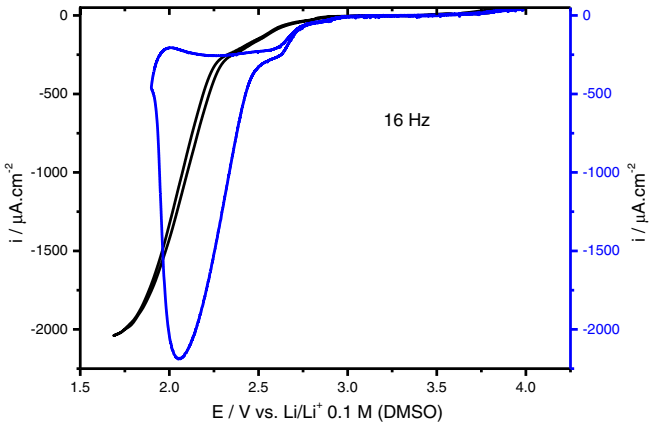


**Figure 2.** Cyclic scan voltammetry of 2 mM FePc in $O_2$ saturated 0.1M - TBA-$PF_6$ in DMSO (black) and in $O_2$ saturated 0.1M LiTFSI in DMSO (blue) at a 0.2 $cm^2$ Au RDE at 16 Hz and v = 20 mV.$s^{-1}$.

yields a diffusion coefficient of FePc in DMSO $D_{FePc} = 5.22 \times 10^{-7}$ $cm^2s^{-1}$.; much less than the diffusion coefficient of $O_2$ in the same solvent, $D_{O_2} = 1.67 \times 10^{-5}$ $cm^2s^{-1}$.[30]

An analysis of the Levich slopes for the ORR in absence of lithium ions but in 2 mM FePc and 2 mM $O_2$ are consistent with a diffusion constant close to the value for molecular oxygen and much larger than soluble FePc. Therefore the convective-diffusion of oxygen toward the electrode results in a catalytic current with an EC' type mechanism (catalytic electrochemical-chemical type mechanism ) with the redox catalysis of the reduced FePc(I) species.[31] Oxygen diffuses toward the Au electrode where it meets the reduced FePc(I) at the electrode surface regenerating FePc(II) and forming $O_2^-$.

It should be stressed here the difference with aqueous solutions since FePc supported on carbon shows ORR coincident with the first redox couple, Fe(III)/Fe(II) with a redox catalysis mechanism:[19]

$$PcFe(III)OH + H_2O + e \rightarrow PcFe(II)OH_2 + HO^- \quad [6]$$

$$PcFe(II)OH_2 + O_2 \rightarrow PcFe(II)O_2^- + H_2O \quad [7]$$

However, in non-aqueous solvents such as DMSO that strongly coordinate as axial ligand the Fe center of the FePc the ORR takes place at 1.5 V more reducing potentials than in aqueous solutions in the second redox couple Fe(II)/Fe(I) potential range as can be seen in Figure 1. This important difference has been overlooked in previous reports.[4,12] We rationalize this behavior by assuming that in order to displace a strong dipole like DMSO from the Fe center in the phtalocyanine a strongly charged species needs to be formed, such as superoxide and that a second electron is needed to polarize the molecule.

In Figure 2 we compare the ORR on a rotating Au disk electrode (RDE) in 2 mM Fe(II)Pc in DMSO containing TBA-$PF_6$ and LiTFSI respectively. We notice in the absence of $Li^+$ ions a well-defined $O_2$ reduction wave which reaches the Levich convective-diffusion limiting current for a one-electron reduction process. In the presence of 0.1 M LiTFSI, however, the $O_2$ reduction wave is shifted to positive potentials by 250 mV and exhibits a peak and 2.05 V with current densities very close to the convective diffusion level for a one-electron ORR (see Figure in Supporting Information). Furthermore, the Au cathode is not passivated in Figure 3b by the oxygen reduction products as seen by the cathodic currents in the back-scan. In the same 0.1 M LiTFSI –DMSO electrolyte without Fe(II)Pc (Figure 3a), however, the ORR peak currents are always below the convective-diffusion limiting current and surface passivation by the ORR is observed.[23]

At each rotation frequency the peak current increases linearly with the oxygen partial pressure at constant FePc concentration and with rotation frequency at constant concentration of oxygen and FePc as shown in Supporting Information. Since the oxygen solubility in DMSO is 2 mM at $p_{O_2} =$ 1atm $O_2$ a 1:1 oxygen to FePc concentration ratio in solution is attained under oxygen saturation and 2 mM FePc in solution.

The reduction of oxygen in DMSO containing Li ions in absence of the soluble FePc catalyst, has been extensively studied and follows two limiting mechanisms:[32–35] (a) a surface reaction leading to thin conformal $Li_2O_2$ films, and (b) a solution phase mechanism via disproportionation of soluble lithium superoxide with formation of large $Li_2O_2$ particles. The surface mechanism at high current densities and low donor number solvent favors thin film growth with passivation of the active cathode:

$$O_2 + Li^+ + e \rightarrow [O_2Li]_{surf} \quad [8]$$

$$[O_2Li]_{surf} + [O_2Li]_{surf} \rightarrow Li_2O_2 + O_2 \quad [9]$$

$$[O_2Li]_{surf} + Li^+ + e \rightarrow Li_2O_2 \quad [10]$$

while, the solution phase mechanisms prevails at low current density and high donor number solvents:

$$O_2 + Li^+ + e \rightarrow [O_2Li]_{soln} \quad [11]$$

$$2[O_2Li]_{soln} \rightarrow Li_2O_2\,(particle) \quad [12]$$

The discharge product of the ORR in $Li^+$ containing aprotic solvents, $Li_2O_2$ and decomposition products of solvent and anions poorly conducting solids are very hard to oxidize during the charging cycle. This results in high charging overpotential and mass accumulation in successive EQCM reduction-oxidation cycles.[22,36]

Figure 3A depicts a typical cyclic voltammetry of ORR in $O_2$ saturated 0.1 M LiTFSI/DMSO electrolyte and the simultaneous EQCM mass evolution. Notice the passivation of the electrode surface as the current in the reverse scan is almost negligible after the $O_2$ reduction peak. However when 2 mM soluble FePc catalyst is present in the $O_2$ saturated electrolyte the reduction current density and EQCM mass uptake during ORR are much larger, and there is no passivation of the electrode surface as shown in Figure 3B. A comparison of the mass gained in Figs. 3A and 3B shows a larger $Li_2O_2$ deposit and its complete removal upon oxidation below 4.0 V when soluble FePc is present in the electrolyte. In the absence of FePc the mass can only be recovered at very high overpotential with simultaneous oxidation of the solvent DMSO.[22,37,38]

Notice that the potential at which we observe mass decay during oxidation in FePc containing solutions coincides with formation of Fe(III)Pc above 3.5 V (dashed line in Fig. 3B) This is consitent with the results reported by Sun et al.[12] An important difference in FePc solution is the mass drop above 3.5 V in the latter case.

A broad cathodic small pre-peak at 2.65 V in Figures 2 and 3 has been observed due to soluble species since there is no mass increase at this potential and is seen only if the FePc solutions contain dissolved oxygen, even in the absence of lithium. The nature of this pre-peak, which has been reported previously by Sun et al.[12] and has been associated it to FePc-$O_2$, is not clear at all. This pre-peak could be due to a spurious reaction like traces of water protonating superoxide which would disproportionate into soluble $H_2O_2$ and $O_2$. Alternatively, since at the pre-peak there is no EQCM mass increase nor detection of soluble superoxide with a rotating ring-disk electrode (RRDE) as shown below we associate the pre-peak to a spurious reaction in the presence of traces of water with formation of soluble hydrogen peroxide with the water traces flux limiting the cathodic current.[39]

$$O_2 + H_2O + 2e \rightarrow H_2O_2 + 2HO^- \quad [13]$$

The ORR is tuned to Fe(II)/Fe(I) redox couple at the larger peak about 2.0–2.2 V with simultaneous mass increase unlike in the absence of FePc where the mass gain starts at more positive potentials, c.a

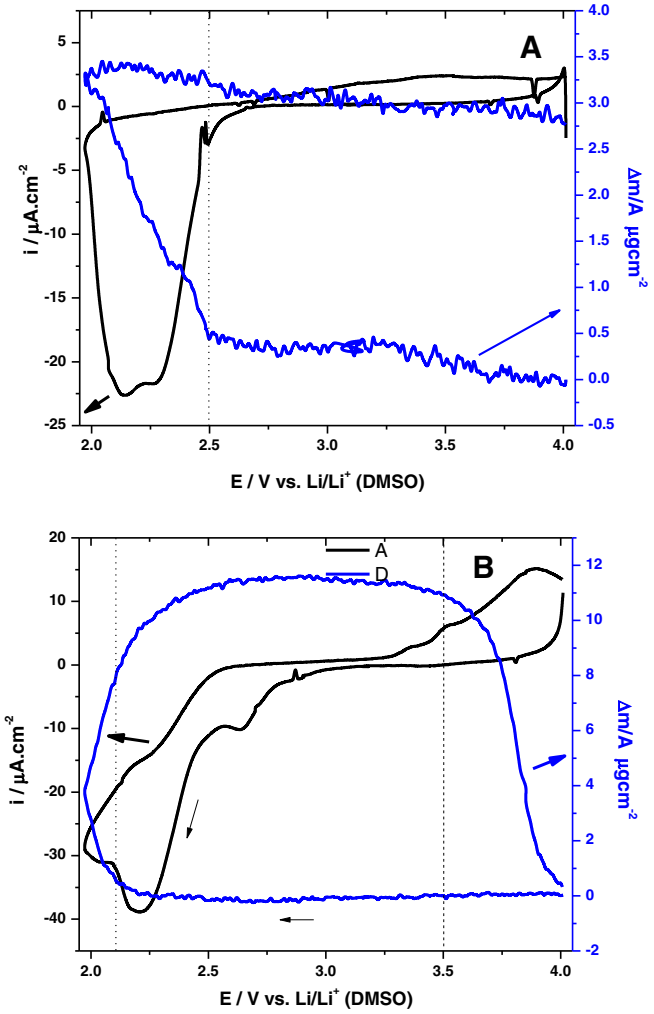


**Figure 3.** Cyclic voltammetry and simultaneous EQCM mass variation in 0.1 M LiTFSI-DMSO in $O_2$ saturated solution: (A) in the absence of FePc and (B) in 2mM FePc.

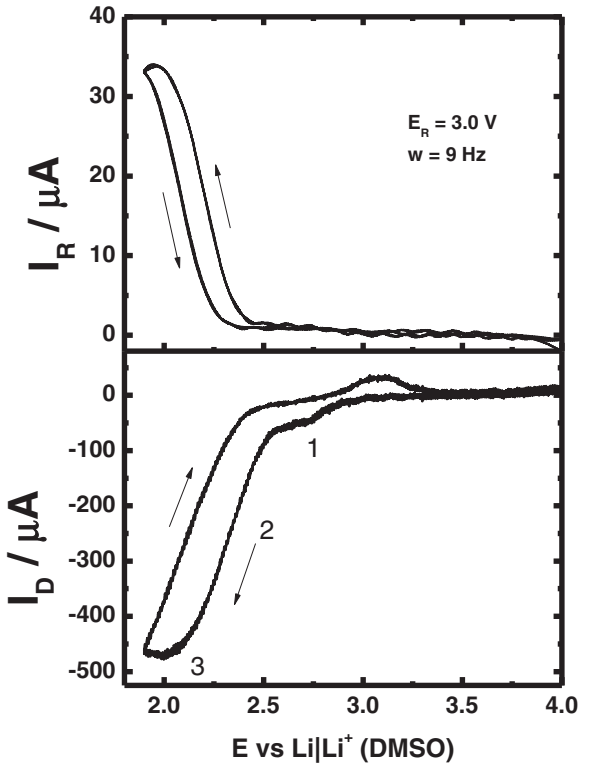


**Figure 4.** Cyclic voltammetry of ORR at Au disk of RRDE at 100 $mV.s^{-1}$ and simultaneous Au ring detection of soluble superoxide. $E_R$ = 3.0 V and W = 9 Hz. in 0 .1 M LiTFSI-DMSO.

2.5 V due to disportionation of soluble superoxide.[40] The electron transfer to the molecular shuttle FePc requires $Li^+$ ions to compensate charge and yields $FePc(II)O_2^{-}{\cdot}Li^+$ .

Detection of soluble superoxide ion with the rotating ring disk electrode (RRDE) simultaneous to the cyclic voltammetry of ORR depicted in Figure 4 exhibits three distinctive potential intervals. At the cathodic pre-peak (1) soluble superoxide cannot be detected at the ring electrode unlike at more reducing potentials (2) where soluble superoxide can be detected at the ring. Notice that the ring current arising from oxygen reduction at the Au disk at 2.0 V close to the convective-diffusion limiting current (3) is only 25% of the expected value from the $O_2$ flux at the disk electrode since $I_R/N_0I_d = 0.25$. Therefore, a fraction of the ORR yields soluble superoxide at the ring electrode.

Unlike cyclic voltammetry where potential and time variables are convoluted, the RRDE chronoamperometry at fixed Au disk electrode potential shows the time evolution of soluble superoxide detected at the ring electrode at each disk electrode potential. Figure 5 depicts selected transient disk and ring currents due to ORR and soluble superoxide oxidation with the onset of superoxide oxidation ring current before a mass increase can be detected (see Figure 3).

Iron phtalocyanine, FePc (mol. wt 568 $g.mol^{-1}$) is a large flat macrocycle molecule and the diffusion of FePc ($D_{FePc}$ ~$2 \times 10^{-7}$ $cm^2s^{-1}$) is hindered unlike soluble $O_2^-$ ($D_{O_2^-} = 1.15 \times 10^{-5}$ $cm^2s^{-1}$ in DMSO). Furthermore, the slope of a Levich convective-diffusion

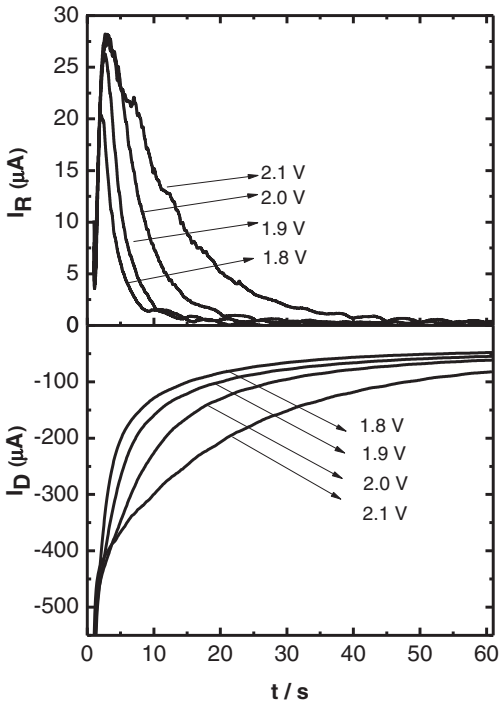


**Figure 5.** RRDE chronoamperometry for the ORR at Au disk at different electrode potentials and soluble superoxide collection at the Au ring at ER = 3.0 V, W = 9 Hz., 2 mM PcFe in 0 .1 M LiTFSI-DMSO.

plot for a one-electron reduction of oxygen (see supporting information) is consistent with the diffusion of molecular oxygen toward the electrode. Therefore, the formation of the $FePcO_2^-$ adduct is expected to take place at the electrode surface in a redox cycle involving reduced FePc and oxygen.

The parameters of the quartz crystal equivalent electrical circuit, R and ωL depend on the electrochemically deposited mass, solvent trapped in pores, viscoelastic properties of the deposit and size and structure of particles deposited on the surface.

The lumped element model quartz crystal impedance approximation is valid for $|Z_S|/Z_q \ll 2.tan(\phi_q/2)$ with $R_S$ and $X_{LS} = \omega L$ the real and imaginary parts of the lumped element impedance $Z_{LEM}$[41]

$$Z_{LEM} \cong \frac{N\pi}{4K^2\omega_S C_O}\left[\frac{Z_S}{Zq} = R_S + jX_{LS}\right] \quad [14]$$

where $K^2$ is the quartz electromechanical coupling coefficient, $\phi_q$ is the complex acoustic wave phase shift across the quartz, Co is the static capacitance of the resonator, $\omega = 2\pi f$ with f the excitation frequency, where the quartz characteristic impedance is $Zq = \sqrt{(\rho q \mu q)}$, $\rho_q$ is the quartz density (2651 Kg $m^{-3}$) and μq the quartz stiffness (2.947. 1010 N.$m^{-2}$). $Z_S$ is the surface mechanical impedance due to the surface ORR insoluble products deposited on the Au coated quartz crystal immersed in viscous DMSO liquid electrolyte while Zq for an AT-cut quartz crystal is 8.849. $10^6$ Kg $m^{-2}s^{-1}$. Near resonance $\omega \cong \omega_o = 2\pi f_o$ , with $f_o$ the series resonance frequency and N is the harmonic resonance number.[42] The validity of the LEM equivalent circuit to within 1% of the Transmission Line Model[40] is fulfilled for the ratio of the surface film and/or liquid impedance ($Z_S$) to the quartz crystal impedance ($Z_Q$) $Z_S/Z_Q < 0.005$, i.e. since $Z_q \sim 535{,}000\ \Omega$ this holds for $Z_S \leq 2675\ \Omega$. This condition is fulfilled in the present work.

The penetration depth, δ of the shear wave emitted by the oscillating quartz crystal in the surrounding viscous liquid electrolyte at the fundamental frequency $f_0$ is given by:

$$\delta = \left(\frac{\eta}{\pi N f_0 \rho}\right)^{\frac{1}{2}} \ 0.45\ \mu m \quad [15]$$

For the fundamental resonance frequency (N = 1) with ρ = 1.104 g.$cm^{-3}$ and η = 1.99 mPa.s for DMSO with an electrical impedance of the bare quartz crystal immersed in the viscous DMSO liquid before ORR deposition of $Li_2O_2$ is $Z_L{}^*$:

$$Z_l^* = \sqrt{\rho_l \eta_l \omega j} = (1+j)\sqrt{\frac{\rho_l \eta_l \omega}{2}} = 326\ \Omega\ (1+j) \quad [16]$$

For the 0.1M $LiPF_6$/DMSO electrolyte solution with the 10 MHz quartz crystal mounted with the o-ring we find experimentally 460 Ω.

For a thin conformal $Li_2O_2$ surface deposit the surface impedance, $Z_S$ is determined by the thickness, $d_f$, density, $\rho_f$, and complex shear modulus, $G_f$, of the film in contact with the viscous liquid:[43]

$$Z_f = R_f + j\omega L_f = \frac{2\omega L_Q}{\pi\sqrt{\mu_Q \rho_Q}}\left(\sqrt{\rho_f G_f}\, tanh\left(j\omega d_f \sqrt{\frac{\rho_f}{G_f}}\right)\right) \quad [17]$$

For a rough or porous surface deposit of particles such as $Li_2O_2$ on Au coated quartz crystal with an average height, h, and particle separation,ξ, or permeability length, which defines the ability of the layer to allow liquid motion through the surface structure during quartz crystal oscillation there are two limiting cases: a) for $\delta >> \xi$ a gravimetric response of the liquid trapped within the structure is observed and is equivalent to the prediction of Sauerbrey equation; and b) for $\delta \leq \xi$ the increased permeability length facilitates liquid motion with dissipation of the oscillation energy in surface pores or grooves of the $Li_2O_2$ deposit.[44–46]

A typical potential step experiment at 2.3 V in the ORR region is depicted in Figure 6 with a linear mass increase during ORR and total mass recovery in FePc solution during oxidation at a potential as low as 3.6 V in the DMSO stability range, but constant mass in

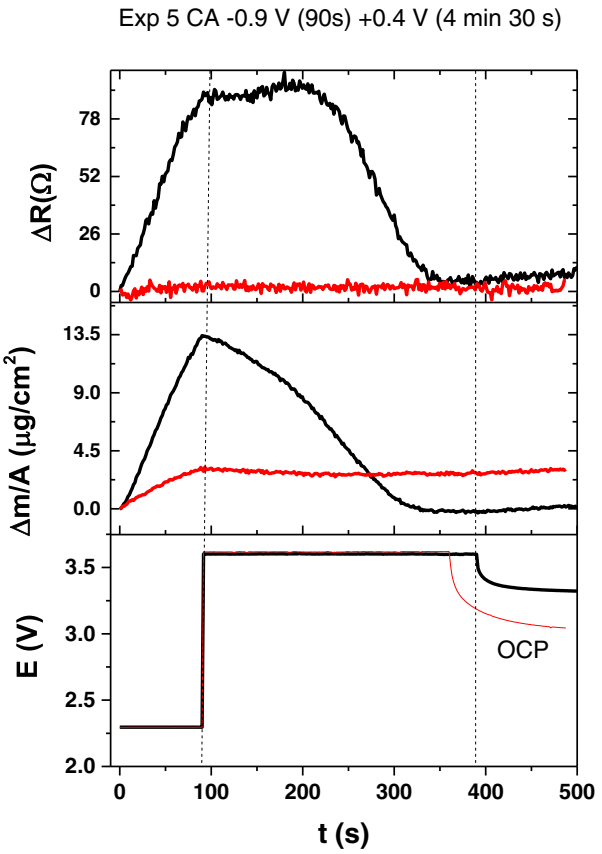


**Figure 6.** Potential steps for ORR and OEM (A) simultaneous to the mass (B) and ΔR (C) transients.

FePc free electrolyte.[38] In the absence of FePc in solution the EQCM dissipation parameter ΔR is almost zero under gravimetric conditions and the mass uptake in the presence of FePc catalyst is larger than in its absence.

With FePc in solution the dissipation parameter $\Delta R < \Delta\omega L$ increases linearly following the mass uptake due to a gradual growth of particles resulting from the ORR on the surface under conditions where the $\delta \leq \xi$. fulfils. It is of note that the mass decreases at 210 s almost to half of the maximum value while the shear wave dissipation parameter, ΔR, is constant and drops at longer times probably due to the dissolution of small $Li_2O_2$ particles at short time accounting for mass drop but not for dissipation due to the larger particles at the surface,.[47,48]

A current step experiment at −150 μA.$cm^{-2}$ (Figure 7) shows that the mass and the shear wave dissipation ΔR parameter increase during oxygen reduction, with a lag phase due to the accumulation of soluble $O_2^-$ species at the electrode surface until formation of a solid insoluble $Li_2O_2$ deposit as explained elsewhere for FePc free electrolyte.[22] During oxidation at 150 μA.$cm^{-2}$ an almost a complete mass recovery is observed before reaching 4.2 V where DMSO is electrochemically stable,[38] and the shear wave dissipation in DMSO electrolyte of the oscillating bare Au coated quartz crystal is also recovered after the surface insoluble deposit has been removed completely. Here ΔR and ΔωL (proportional to Δm/A) follow each other under a constant flux of electrons imposed by the applied constant current.

Notice in Figure 7 that the $O_2$ reduction charge is larger than the oxidation charge unlike the mass deposited that is fully recovered upon oxidation. This might be due to soluble superoxide which is lost by diffusion into solution or to the degradation of solvent and electrolyte by the oxygen reduction highly reactive intermediates.

The mass uptake during ORR at different current densities is compared in Figure 8, with a linear growth after some incubation time lag

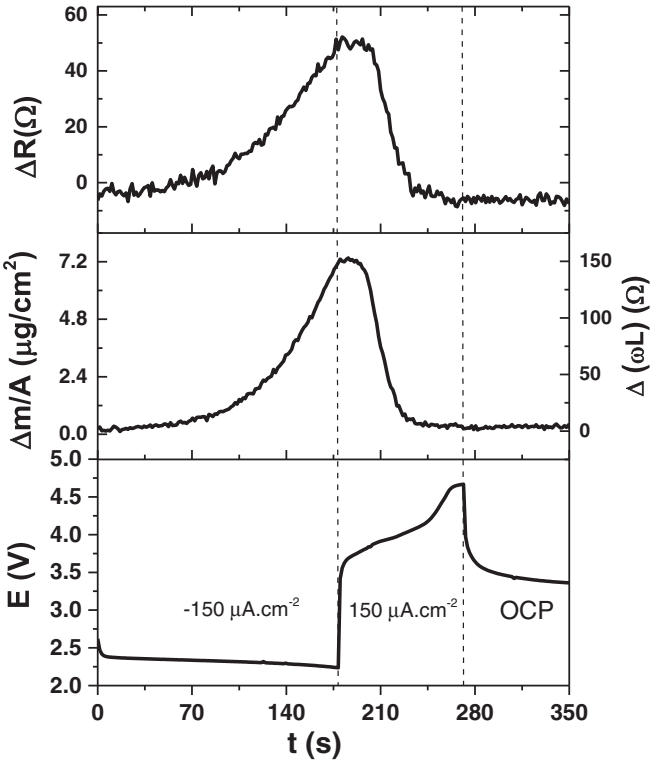


**Figure 7.** Galvanostatic pulses at ±150 mAcm$^{-2}$ of ORR on Au electrode in 0 .1 M LiTFSI-DMSO. Dissipation ΔR EQCM parameter (upper panel), Δm/A and $\Delta X_L$ (middle panel) and E (lower panel).

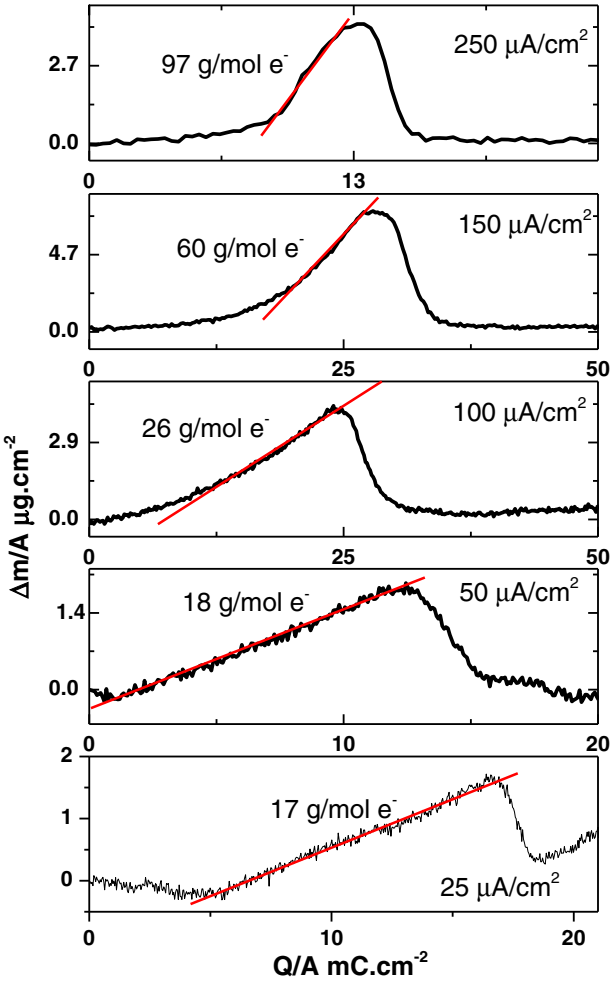


**Figure 8.** Mass to charge plots for galvanostatic pulses at different current density.

which decreases at higher current densities. The resulting mass per electron (m.p.e.) is close to the expected value 23 gram per Faraday for $Li_2O_2$ , at low current density while at current densities above 100 μA.cm$^{-2}$ the mass grows more sharply and the m.p.e. is much larger than expected for $Li_2O_2$, which can be explained by partial solvent co-deposition or trapping in the solid deposit at high deposition rate as discussed in a previous communication.[49] The shear wave dissipation parameter, ΔR, also exhibits a delay with respect to the mass evolution during constant current oxidation.

The 1:1 $O_2$ to FePc stoichiometry has been verified by studying the effect of soluble FePc concentration and oxygen partial pressure. The effect of FePc concentration on the cathodic current and mass uptake in the discharge step can be seen in Figure 9. The charge and mass deposited increase with the soluble FePc concentration below the oxygen solubility in DMSO, 2.10 mM.[30] and a linear plot of the cathodic charge vs. FePc concentration is found (see Supporting Information).

On the other hand, the mass decay during oxidation takes place even at the lowest FePc concentrations with a similar redox mechanisms as reported for $TTF^+$.[4] Also the shear wave dissipation ΔR, in Figure 9, increases with the amount of the $Li_2O_2$ deposit as expected for a rough surface interacting with a viscous liquid and dissipating shear energy.[50] In the oxidation back scan the larger the soluble FePc concentration, the larger the oxidation current peak at 3.6 V and the faster the mass recovery.

The EQCM mass and shear wave dissipation, RDE and RRDE evidences presented here are consistent with the mechanism for the FePc based solution-phase catalyst which is very effective in the discharge/charge of the Li-$O_2$ battery and also enhances its capacity and cyclability.

The solvent dimethyl sulfoxide as axial ligand stabilizes Fe(II)Pc(DMSO)$_2$. At the Fe(II) Pc/Fe(I)Pc redox potential below 2.5 V (see Fig. 1) superoxide can displace one of the solvent molecules axially coordinated to the Fe atom:

$$Fe(II)\,Pc(DMSO)_2 + O_2 + \mathrm{e} \rightarrow Fe(II)\,Pc(DMSO)O_2^- + DMSO \quad [18]$$

and in $Li^+$ containing solution:

$$Fe(I)\,Pc(DMSO)_2 + O_2 + Li^+ + \mathrm{e} \rightarrow Fe(II)\,Pc\,(\mathrm{DMSO})\,O_2^- Li^+ + DMSO \quad [19]$$

The first electron transfer below 2.5 V corresponds to the soluble species without mass increase but with formation of soluble superoxide detected by the RRDE unlike the iron phtalocyanine free solution. At more reducing potential a mass increase is observed due to the formation of insoluble $Li_2O_2$ as detected by the EQCM mass increase and the Fe(II)Pc(DMSO)$_2$ is recycled to react with $O_2$.

$$Fe(II)\,Pc\,(\mathrm{DMSO})\,O_2^- Li^+ + e + Li^+ + DMSO \rightarrow Fe(II)Pc(DMSO)_2 + Li_2O_2 \downarrow \quad [20]$$

or,

$$Fe(II)\,Pc\,(\mathrm{DMSO})\,O_2^- Li^+ + DMSO \rightarrow Fe(II)Pc(DMSO)_2 + LiO_2 \quad [21]$$

Alternatively, superoxide dismutation may form the insoluble lithium peroxide at the crystal surface.

$$2Fe(II)\,PcO_2^- Li^+ \rightarrow 2PcFe(II)\,Pc + Li_2O_2 + O_2 \quad [22]$$

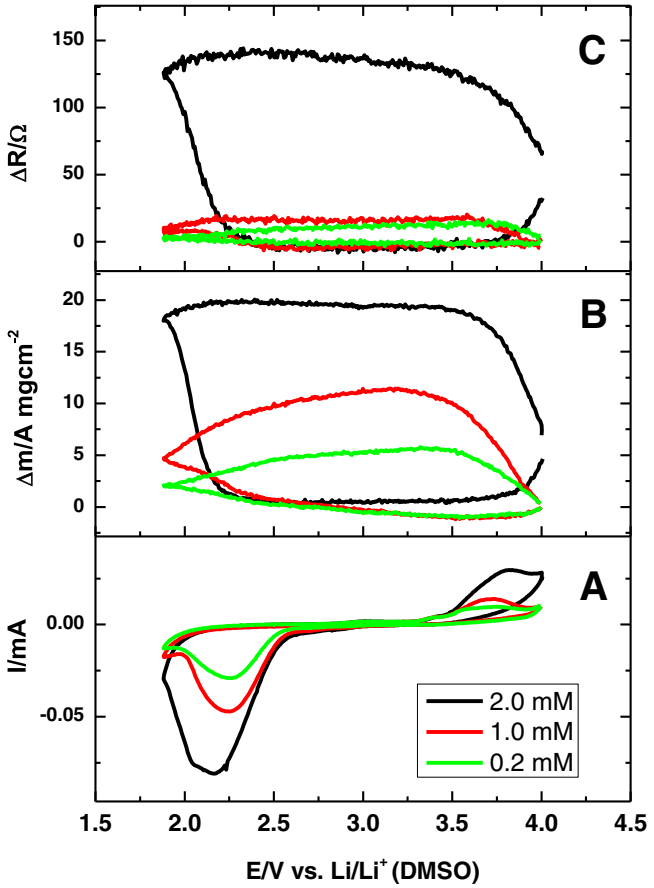


**Figure 9.** A) Cyclic voltammetry of ORR at different soluble FePc concentration in 0 .1 M LiTFSI-DMSO at 20 $mV.s^{-1}$. B) Δm/A areal mass evolution and C) ΔR vs. E.

The following Scheme 2 represents a mechanism consistent with the EQCM and rotating disk and ring disk experimental evidence for the ORR catalysed by soluble FePc.

After formation of $FePcO_2^-$ there is a branching point where part of the superoxide diffuses away into the electrolyte and is detected at the ring electrode and part is further reduced in the presence of lithium ions to yield FePc-LiOOLi which then precipitates onto the electrode as $Li_2O_2$ and results in a mass gain as sensed by the EQCM.

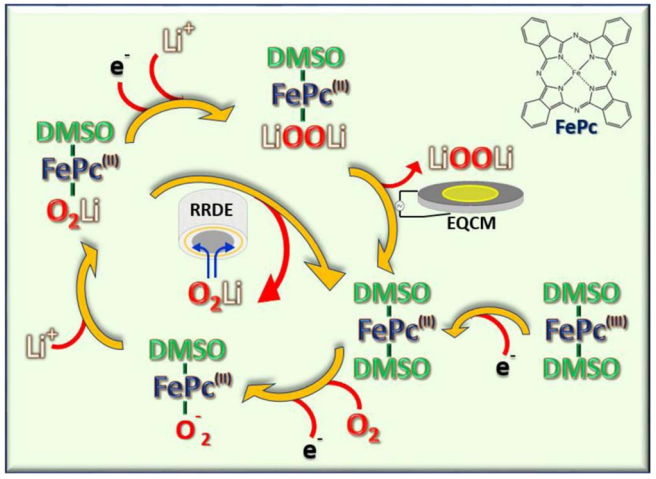


**Scheme 2.** Reaction scheme for the FePc catalyzed ORR.

## Conclusions

Using EQCM and RRDE we have confirmed that the FePc shuttle favors the solution phase mechanism during ORR by one-electron reaction with further formation of insoluble $Li_2O_2$ at the electrode surface. In DMSO electrolyte the ORR takes place at potentials within the $Fe^{II}/Fe^{I}$ redox couple, unlike in aqueous solutions where the $Fe^{III}/Fe^{II}$ redox couple is the redox catalytic reaction in the ORR.

The EQCM gravimetry shows a mass per electron (mpe) close to the value 23 g/mol for the formation of $Li_2O_2$ at low current densities, but a larger mpe value at higher current densities probably due to solvent co-deposition or trapped DMSO in the surface deposit. Lithium superoxide has been detected in RRDE experiments and explains the larger charge during oxygen reduction than in the recharge oxidation cycle, even with total surface mass recovery below 4 V.

In the absence of FePc there is negligible shear wave dissipation and the mass deposited due to conformal $Li_2O_2$ thin film formation during oxygen reduction is less than that observed with the redox shuttle FePc for solution phase ORR with formation of large $Li_2O_2$ deposit.

Shear wave dissipation results are consistent with formation of a surface deposit with an average height, h of few nanometers as measured by AFM and a shear wave decay length, δ, close to the particle separation, ξ, or permeability length, ($\delta \leq \xi$) with liquid motion through the surface structure during quartz crystal oscillation and energy dissipation

During oxidation of the FePc, removal of the surface products is observed as mass loss at low overpotential in the potential range of the $Fe^{III}/Fe^{II}$ redox couple by a redox dissolution mechanism similar to other redox mediators such as TTF.[4] Total mass recovery at 3.6 V in the stability range of DMSO is due to the action of Fe(III)Pc as a chemical scavenger by dissolving insoluble $Li_2O_2$ and reducing the battery re-charging potential.

## Acknowledgments

Funding from UBA, CONICET and ANPCyT PICT 2014V No. 36542 are gratefully acknowledged. WT and FD have a doctoral fellowship and A.Y.T a postdoctoral fellowship from CONICET which are gratefully acknowledged.

## References

1. K. M. Abraham, *Lithium Batteries: Advanced Technologies and Applications*, John Wiley & Sons, Inc (2013).
2. Y. Chen, S. A. Freunberger, Z. Peng, O. Fontaine, and P. G. Bruce, *Nature Chemistry*, **5**, 489 (2013).
3. S. Schaltin, G. Vanhoutte, M. Wu, F. BardÃ©, and J. Fransaer, *Physical Chemistry Chemical Physics*, **17**, 12575 (2015).
4. W. R. Torres, S. E. Herrera, A. Y. Tesio, M. D. Pozo, and E. J. Calvo, *Electrochimica Acta*, **182**, 1118 (2015).
5. M. J. Lacey, J. T. Frith, and J. R. Owen, *Electrochemistry Communications*, **26**, 74 (2013).
6. A. W. Lodge, M. J. Lacey, M. Fitt, N. Garcia-Araez, and J. R. Owen, *Electrochimica Acta*, **140**, 168 (2014).
7. L. Yang, J. T. Frith, N. Garcia-Araez, and J. R. Owen, *Chemical Communications*, **51**, 1705 (2015).
8. H. D. Lim, H. Song, J. Kim, H. Gwon, Y. Bae, K. Y. Park, J. Hong, H. Kim, T. Kim, Y. H. Kim, X. LeprÃµ, R. Ovalle-Robles, R. H. Baughman, and K. Kang, *Angewandte Chemie - International Edition*, **53**, 3926 (2014).
9. A. Y. Tesio, D. Blasi, M. Olivares-Marín, I. Ratera, D. Tonti, and J. Veciana, *Chemical Communications*, **51**, 17623 (2015).
10. J. K. Feng, X. P. Ai, Y. L. Cao, and H. X. Yang, *Electrochemistry Communications*, **9**, 25 (2007).
11. Y. G. Zhu, C. Jia, J. Yang, F. Pan, Q. Huang, and Q. Wang, *Chemical Communications*, **51**, 9451 (2015).
12. D. Sun, Y. Shen, W. Zhang, L. Yu, Z. Yi, W. Yin, D. Wang, Y. Huang, J. Wang, D. Wang, and J. B. Goodenough, *Journal of the American Chemical Society*, **136**, 8941 (2014).
13. H. Jahnke, M. Schönborn, and G. Zimmermann, *Topics in current chemistry*, **61**, 133 (1976).
14. M. Savy, P. Andro, C. Bernard, and G. Magner, *Electrochimica Acta*, **18**, 191 (1973).
15. M. Savy, C. Bernard, and G. Magner, *Electrochimica Acta*, **20**, 383 (1975).
16. J. A. R. van Veen and C. Visser, *Electrochimica Acta*, **24**, 921 (1979).
17. F. Beck, *Journal of Applied Electrochemistry*, **7**, 239 (1977).

18. J. E. Newton and M. B. Hall, *Inorganic Chemistry*, **23**, 4627 (1984).
19. J. Zagal, P. Bindra, and E. Yeager, *Journal of the Electrochemical Society*, **127**, 1506 (1980).
20. A. A. Tanaka, C. Fierro, D. Scherson, and E. B. Yeager, *Journal of Physical Chemistry*, **91**, 3799 (1987).
21. S. Zecevic, B. Simic-Glavaski, E. Yeager, A. B. P. Lever, and P. C. Minor, *Journal of Electroanalytical Chemistry*, **196**, 339 (1985).
22. W. R. Torres, L. Cantoni, A. Y. Tesio, M. del Pozo, and E. J. Calvo, *Journal of Electroanalytical Chemistry*, (2015).
23. W. Torres, N. Mozhzhukhina, A. Y. Tesio, and E. J. Calvo, *Journal of the Electrochemical Society*, **161**, A2204 (2014).
24. G. Z. Sauerberey, *Z. Phys.*, **155**, 206 (1959).
25. N. Mozhzhukhina, M. P. Longinotti, H. R. Corti, and E. J. Calvo, *Electrochimica Acta*, **154**, 456 (2015).
26. D. G. Kwabi, M. Tułodziecki, N. Pour, D. M. Itkis, C. V. Thompson, and Y. Shao-Horn, *Journal of Physical Chemistry Letters*, **7**, 1204 (2016).
27. A. B. P. Lever and J. P. Wilshire, *Inorganic Chemistry*, **17**, 1145 (1978).
28. C. Ercolani, M. Gardini, F. Monacelli, G. Pennesi, and G. Rossi, *Inorganic Chemistry*, **22**, 2584 (1983).
29. K. M. Kadish, L. A. Bottomley, and J. S. Cheng, *Journal of the American Chemical Society*, **100**, 2731 (1978).
30. C. O. Laoire, S. Mukerjee, K. M. Abraham, E. J. Plichta, and M. A. Hendrickson, *Journal of Physical Chemistry C*, **114**, 9178 (2010).
31. R. S. Nicholson and I. Shain, *Analytical Chemistry*, **36**, 706 (1964).
32. B. D. Adams, C. Radtke, R. Black, M. L. Trudeau, K. Zaghib, and L. F. Nazar, *Energy and Environmental Science*, **6**, 1772 (2013).
33. N. B. Aetukuri, B. D. McCloskey, J. M. Garciá, L. E. Krupp, V. Viswanathan, and A. C. Luntz, *Nature Chemistry*, **7**, 50 (2015).
34. L. Johnson, C. Li, Z. Liu, Y. Chen, S. A. Freunberger, P. C. Ashok, B. B. Praveen, K. Dholakia, J. M. Tarascon, and P. G. Bruce, *Nature Chemistry*, **6**, 1091 (2014).
35. M. Safari, B. D. Adams, and L. F. Nazar, *Journal of Physical Chemistry Letters*, **5**, 3486 (2014).
36. F. Marchini, S. Herrera, W. Torres, A. Y. Tesio, F. J. Williams, and E. J. Calvo, *Langmuir*, **31**, 9236 (2015).
37. S. E. Herrera, A. Y. Tesio, R. Clarenc, and E. J. Calvo, *Physical Chemistry Chemical Physics*, **16**, 9925 (2014).
38. N. Mozhzhukhina, L. P. Mendez De Leo, and E. J. Calvo, *Journal of Physical Chemistry C*, **117**, 18375 (2013).
39. N. B. Aetukuri, B. D. McCloskey, J. M. Garciá, L. E. Krupp, V. Viswanathan, and A. C. Luntz, *Nature Chemistry*, **7**, 50 (2015).
40. M. del Pozo, W. Torres, S. Herrera, and E. J. Calvo, *ChemElectroChem*, in press, 1537 (2016).
41. A. Arnau, Y. Jimenez, R. Fernández, R. Torres, M. Otero, and E. J. Calvo, *Journal of the Electrochemical Society*, **153**, C455 (2006).
42. S. J. Martin, V. E. Granstaff, and G. C. Frye, *Analytical Chemistry*, **63**, 2272 (1991).
43. V. E. Granstaff and S. J. Martin, *Journal of Applied Physics*, **75**, 1319 (1994).
44. M. D. Levi, N. Shpigel, S. Sigalov, V. Dargel, L. Daikhin, and D. Aurbach, *Electrochimica Acta*, **232**, 271 (2017).
45. N. Shpigel, M. D. Levi, S. Sigalov, O. Girshevitz, D. Aurbach, L. Daikhin, P. Pikma, M. Marandi, A. Jänes, E. Lust, N. Jäckel, and V. Presser, *Nature Materials*, **15**, 570 (2016).
46. L. Daikhin, S. Sigalov, M. D. Levi, G. Salitra, and D. Aurbach, *Analytical Chemistry*, **83**, 9614 (2011).
47. D. Zhai, H. H. Wang, J. Yang, K. C. Lau, K. Li, K. Amine, and L. A. Curtiss, *Journal of the American Chemical Society*, **135**, 15364 (2013).
48. S. Lau and L. A. Archer, *Nano Letters*, **15**, 5995 (2015).
49. W. R. Torres, A. Y. Tesio, and E. J. Calvo, *Electrochemistry Communications*, **49**, 38 (2014).
50. B. D. McCloskey, C. M. Burke, J. E. Nichols, and S. E. Renfrew, *Chemical Communications*, **51**, 12701 (2015).